ACS APPLIED ELECTRONIC MATERIALS

Article

Cite This: ACS Appl. Electron. Mater. 2019, 1, 869−876

pubs.acs.org/acsaelm

Electronic Transport Evidence for Topological Nodal-Line Semimetals of ZrGeSe Single Crystals

Lei Guo,[†,§] Ting-Wei Chen,[‡] Chen Chen,[†] Lei Chen,[§,∥] Yang Zhang,[†] Guan-Yin Gao,[⊥] Jie Yang,[#] Xiao-Guang Li,[⊥] Wei-Yao Zhao,*[,§,∥] Shuai Dong,*[,†] and Ren-Kui Zheng*[,‡,§]

[†]School of Physics, Southeast University, Nanjing 211189, China

[‡]School of Materials Science and Engineering and Jiangxi Engineering Laboratory for Advanced Functional Thin Films, Nanchang University, Nanchang 330031, China

[§]State Key Laboratory of High Performance Ceramics and Superfine Microstructure, Shanghai Institute of Ceramics, Chinese Academy of Sciences, Shanghai 200050, China

[∥]ISEM, Innovation Campus, University of Wollongong, Wollongong, NSW 2500, Australia

[⊥]Hefei National Laboratory for Physical Sciences at the Microscale, Department of Physics, and Collaborative Innovation Center of Advanced Microstructures, University of Science and Technology of China, Hefei 230026, China

[#]Suzhou Institute of Nano-Tech and Nano-Bionics, Chinese Academy of Sciences, Suzhou 215123, Jiangsu, China

Supporting Information

ABSTRACT: Although the band topology of ZrGeSe has been studied via the magnetic torque technique, the electronic transport behaviors related to the relativistic fermions in ZrGeSe are still unknown. Here, we first report systematic electronic transport properties of high-quality ZrGeSe single crystals under magnetic fields up to 14 T. Resistivity plateaus of temperature-dependent resistivity curves in both the presence and absence of magnetic fields as well as large, nonsaturating magnetoresistance in the low-temperature region were observed. By analyzing the temperature- and angular-dependent Shubnikov−de Haas oscillations and fitting it via the Lifshitz−Kosevich (LK) formula with the Berry phase being taken into account, we proved that Dirac fermions dominate the electronic transport behaviors of ZrGeSe and the presence of the nontrivial Berry phase. First-principles calculations demonstrate that ZrGeSe possesses Dirac bands and normal bands near Fermi surface, resulting in the observed magnetotransport phenomena. These results demonstrate that ZrGeSe is a topological nodal-line semimetal, which provides a fundamentally important platform to study the quantum physics of topological semimetals.

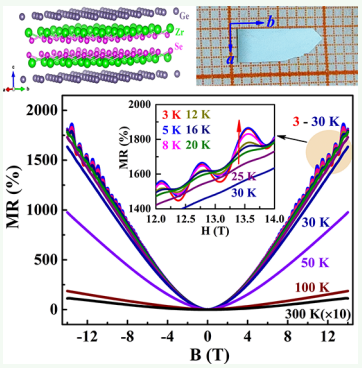

KEYWORDS: *transport properties, topological nodal-line semimetal, Shubnikov−de Haas oscillations, Fermi surface, DFT calculation, band topology*

1. INTRODUCTION

The topological state of quantum materials is now one of the spotlights in condensed matter physics and materials science and has attracted tremendous attention as of now. Different types of band topology in quantum materials have been predicted and investigated since the first report of topological insulators a decade ago.[1,2] Under ideal conditions, the Fermi surface, which determines the electronic transport properties of topological quantum materials, is composed of isolated band crossing points and/or lines, which is different from those of normal conductors.[3,4] Because of the peculiar Fermi surface, topological quantum materials possess plenty of quantum phenomena such as extremely large magnetoresistance, ultrahigh carrier mobility, quantized Hall effect, and chiral anomaly in magnetoresistance, which not only are fundamentally important but also provide potential device applications.[5,6] Besides bulk gapped topological insulators, bulk gapless topological semimetals have been progressively discovered in recent years. According to the degeneracy and distribution of band-crossing points in the Brillouin zone, topological semimetals are classified into Weyl semimetals, Dirac semimetals, and nodal-line semimetals.[7−11] Among them, Dirac semimetals are usually regarded as a three-dimensional graphene, which possesses band crossing points with 4-fold degeneracy near the Fermi energy (E_F). Alternatively, the Dirac points degenerate to pairs of discrete Weyl points with double degeneracy and different chirality (relevant materials are denoted as Weyl semimetals).[7−9] For nodal-line semimetals, the band crossing forms closed loops instead of discrete points in the Brillouin zone.[10−12] Theoretical calculations predicted that the spin−orbital coupling may lead the nodal ring to evolve into Weyl nodes

Received: January 31, 2019
Accepted: May 13, 2019
Published: May 13, 2019

DOI: 10.1021/acsaelm.9b00061
ACS Appl. Electron. Mater. 2019, 1, 869−876

or Dirac nodes or open a gap to form a topological insulator, thus making nodal-line semimetal become one of the fundamental materials in topological physics studies.[12,13]

Several single crystals have been predicted to be nodal-line semimetals, including Ca_3P,[14] Ca_3P_2,[15] A_2B (A = Ca, Sr, and Ba; B = As, Sb, and Bi),[16] Mg_3Bi_2,[17] LaN,[18] $Cu_3(Pd,Zn)N$,[19,20] (Tl,Pb)$TaSe_2$,[21,22] ZrSiS,[23−27] CaAg(P,As),[28] and $BaMX_3$ (M = V, and Nb, Ta; X = S and Se).[29] Unfortunately, experimental progress on nodal-line semimetals is quite limited. Particularly, electronic transport evidence is only presented in very limited materials, and direct confirmation of the existence of nodal rings is verified only in $PbTaSe_2$[22] and ZrSiS[27] compounds by angle-resolved photoemission spectroscopy (ARPES). Among the aforementioned semimetals, ZrSiS attracts the most attention for its distinguished band structure and interesting transport properties. In ZrSiS, all energy bands crossing the Fermi surface are Dirac bands (linearly dispersed over a larger energy range than any other quantum materials), which implies that one can study behaviors of pure Dirac electron without interference from normal electrons.[27] In addition, ZrSiS harbors two types of unusual Dirac cones: the first one forms the known closed loop near the Fermi level, and the other, generated by a square Si lattice protected by nonsymmorphic symmetry, will not open a gap regardless of the strength of spin−orbit coupling.[27] Because ZrSiS is quite popular recently, it is necessary to investigate some isostructural materials. Hu et al.[30] have studied the Fermi surface of the ZrSiSe and ZrSiTe via the de Haas−van Alphen (dHvA) quantum oscillations and deduced that both materials are nodal-line semimetal candidates. A similar method has been applied to study ZrGeM (M = S, Se, and Te)[31] and ZrSnTe[32] single crystals whose dHvA quantum oscillations witness the possible existence of nodal-line fermions in this family of materials.

The dHvA quantum oscillations is an important technique for extracting the relativistic nature of Dirac fermions in topological quantum materials and has its own advantages (e.g., no carrier scattering is involved). It is also important to understand the electronic transport properties of topological semimetals for the purpose of basic research and device applications which usually take advantage of electronic properties. Motivated by this, we significantly optimized the quality of ZrGeSe single crystals and systematically investigated the electronic transport properties of these single crystals which show resistance plateaus in both the absence (H = 0 T) and presence of a magnetic field ($0 < H \leqslant 14$ T) and large nonsaturating magnetoresistance in the low-temperature region ($3\ \mathrm{K} \leqslant T \leqslant 50$ K). By analyzing the Shubnikov−de Haas (SdH) oscillations of the magnetoresistance obtained at fixed low temperatures, we deduced that the nodal-line fermions dominate the electronic transport behaviors and the presence of the nontrivial Berry phase in ZrGeSe single crystals. On the other hand, the findings of large nonsaturating magnetoresistance and high mobility in this van der Waals single crystal may encourage more basic property studies and device fabrication research.

2. EXPERIMENTAL SECTION

High-quality ZrGeSe single crystals were grown by the chemical vapor transport (CVT) method using the iodine (I_2) as transport agent.[30,31] Briefly, a high-purity stoichiometric amount (~1.5 g) of Zr, Ge, and Se powder (200 mesh), together with 10 mg/mL iodine, is sealed in quartz tube as the starting materials. The crystal growth was performed in a two-zone furnace between 950 °C (source) and 850 °C (sink) for 1 week. The as-grown single crystals exhibit plate-like shape with a typical size of approximately 5−10 mm in length and 3−4 mm in width and the normal vector of [001].

The crystal structure of the single crystals was characterized by a PANalytical X'pert X-ray diffractometer equipped with Cu $K\alpha_1$ radiation. High-resolution transmission electron microscopy (HRTEM) and selected area electron diffraction (SAED) were measured using a Tecnai G2F20 S-Twin transmission electron microscope. Note that the electron beam is incident along the [110] crystallographic direction. The chemical composition and distribution maps of the single crystals were measured via energy dispersive X-ray spectroscopy (EDS) using an X-ray energy dispersive spectrometer (Oxford Aztec X-Max80) installed on the Zeiss Supra 55 scanning electron microscope.

The electronic transport properties were measured by the standard four-probe method using a physical property measurement system (PPMS-14T, Quantum Design). Ohmic contacts were prepared on a fresh cleavage *ab*-plane by using room temperature cured silver paste. The electric current is parallel to the *b*-axis while the direction of the magnetic field is parallel to the *c*-axis of the crystal in the transverse magnetotransport measurement configuration.

The first-principles electronic structure calculations are performed by using the Vienna *ab initio* simulation package (VASP) with the projector augmented-wave (PAW) potentials.[33,34] To acquire an accurate description of the crystalline structure, the Perdew−Burke−Ernzerhof for the solids (PBEsol) functional is adopted.[35] The cutoff of the plane wave basis is fixed to 500 eV, and the Monkhorst−Pack k-point mesh is set to be 11 × 11 × 5 for the minimal cell. Both the lattice constants and atomic positions are fully relaxed until the force on each atom is below 0.01 eV/Å. The Fermi surface is handled with Vaspkit, a post-VASP code, using a 54 × 54 × 24 k-mesh.[36]

3. RESULTS AND DISCUSSION

Characterization of ZrGeSe Single Crystals. Similar to other WHM compounds (W = Zr/Hf/La, H = Si/Ge/Sn/Sb, M = O/S/Se/Te), ZrGeSe possesses a layered tetragonal crystal structure formed by stacking of Se−Zr−Ge−Zr−Se slabs along the *c*-axis (Figure 1a).[37] As a result of the layered

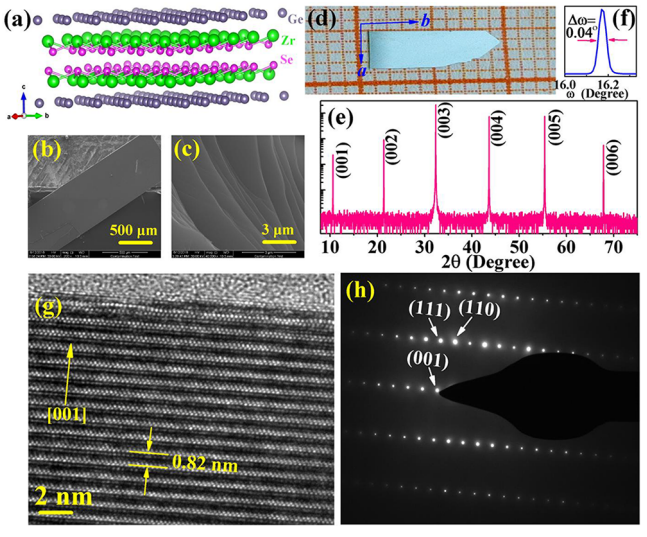

Figure 1. Structure characterization of ZrGeSe single crystals. (a) Crystal structure of ZrGeSe. (b) SEM image of a ZrGeSe single crystal. (c) SEM image of a ZrGeSe single crystal taken near its edge. (d) Photograph of a typical ZrGeSe single crystal with 1 cm in length. (e) XRD patterns of the ZrGeSe. (f) XRD rocking curve taken on the ZrGeSe (003) peak. (g) High-resolution TEM image. (h) Selected area electron diffraction pattern of the ZrGeSe single crystal.

DOI: 10.1021/acsaelm.9b00061
ACS Appl. Electron. Mater. 2019, 1, 869−876

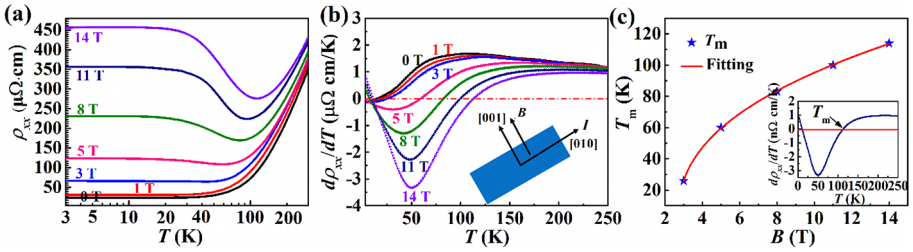

Figure 2. Temperature-dependent transport properties of the ZrGeSe single crystal. (a) Temperature dependence of resistivity in different magnetic fields, as measured by using the schematic geometry shown in the inset of (b). (b) $d\rho_{xx}/dT$ plotted as a function of temperature. (c) T_m plotted as a function of magnetic field. Inset: T_m value obtained from the differential curve.

crystal structure, the obtained ZrGeSe single crystals via the CVT method exhibit a plate-like shape. A large and smooth *ab*-plane and a layered structure near the edge of a crystal can be observed from the SEM images shown in Figures 1b and 1c, respectively. Figure 1d shows a photograph of a typical ZrGeSe single crystal with centimeter in-plane size. The excellent crystalline quality of the single crystal is reflected by the sharp and clean comb-like (00*l*) (l = 1, 2, 3, 4, 5, and 6) X-ray diffraction (XRD) pattern (Figure 1e) and a very small full width at half-maximum (fwhm) (~0.04°) of the XRD rocking curve taken on the (003) diffraction peak (Figure 1f). High-resolution transmission electron microscopy (HRTEM) demonstrates that the microstructure of the single crystal is nearly perfect (Figure 1g), resulting in a sharp selected area electron diffraction pattern (Figure 1h) which can be indexed with the *P*4/*nmm* space group. X-ray energy dispersive spectroscopy (EDS) reveals a uniform distribution of the Zr, Ge, and Se elements, and the atomic ratios of Zr:Ge:Se are 33.8:33.5:32.7 (Figure S1, Supporting Information). All of these results demonstrate the excellent quality of the ZrGeSe single crystal which provides a good platform to study its electronic transport properties.

As shown in Figure 2a, the zero-field resistivity−temperature (R−T) curve of the ZrGeSe crystal shows a monotonic increase within the entire temperature region (3−300 K), which suggests the metallic ground state of the ZrGeSe. For $T \leqslant 10$ K the resistivity shows a slight fluctuation, which is similar to that reported in Cd_3As_2[38] and ZrSiS[39] Dirac semimetals and could be explained in terms of the quantum ballistic transport. The residual resistivity ratio (RRR) is ~14.9 under a zero magnetic field, suggesting that the ZrGeSe crystal possesses a good metallic property. Moreover, the resistivity in the low-temperature region ($T \leqslant 75$ K) can be quite well fitted using the equation $\rho(T) = \rho_0 + AT^n$ with $n \sim 3.1$ (Figure S2), where ρ_0 is the residual resistivity, A is a constant, and n is the parameter indicating scattering mechanisms. The obtained n value (~3.1) is close to that of the ZrSiS crystal ($n \sim 3$).[39] This type of temperature dependence of resistivity, deviating from the pure electronic correlation-dominated scattering mechanism (n = 2) observed in semimetal families,[40] can be attributed to the interband electron−phonon scattering.[39] In the presence of magnetic fields up to 14 T along the *c*-axis, the resistivity plateaus still remain for $T \leqslant 10$ K, which can be clearly seen by using the logarithmic temperature axis (Figure 2a). Moreover, one can find that the application of magnetic fields induces a metal-to-insulator-like transition in the low-temperature region. Specifically, for $B \geqslant 3$ T the resistivity shows a minimum at a certain temperature (T_m) below which the resistivity increases with decreasing temperature. We employ a ($d\rho_{xx}/dT$)−T plot to obtain the T_m values which are the T values at $d\rho_{xx}/dT = 0$ in Figure 2b. The obtained T_{min} value increases monotonically with increasing magnetic fields, as shown in Figure 2c, and can be fitted by the equation $T_{min} \sim (B - B_0)^{1/\nu}$. The parameter ν is ~2.7, which is close to that of a ZrSiS (ν = 3) crystal.[39] This type of magnetic-field-induced metal-to-insulator-like resistivity transition sometimes may result from the gap opening at the band-touching points in semimetals.[39,41] However, in ZrGeSe, the total resistivity magnitude change is quite small, which may be effectively explained by Kohler's rule. We notice that in a semimetal system like WTe_2[42] or $PtSn_4$ and $PdSn_4$,[43] Kohler's rule is successful to attribute the field-induced low-temperature *RT* curves upturn upon cooling. Because Kohler's rule is both powerful and simplified, we employ Kohler's plot on temperature-dependent magnetoresistance (which will be mainly discussed in the next section) shown in Figure S6. We found that to a certain degree Kohler's rule scaling works well in the 3−300 K region, indicating that the carrier's scattering mechanism may be the same at different temperatures. In this case, even though no field-induced energy gap opens, *RT* curves still present local minima at high magnetic field region. We would like to leave this discussion as an open question in the ZrGeSe system; further low temperature and high magnetic field STM study may solve this puzzle.

Magnetoresistance and SdH Quantum Oscillations. The transverse magnetoresistance (MR) is the change of resistance with the magnetic field applied perpendicular to the electric current, which is defined by $MR = \frac{\rho(B) - \rho(0)}{\rho(0)}$, where $\rho(B)$ is the resistivity in an applied magnetic field B. MR measurements could reflect the Shubnikov−de Haas (SdH) oscillations and help to gain insight into the size and shape of the Fermi surface of semimetals. We thus conduct the MR measurements at several fixed temperatures and plot MR as a function of magnetic field in Figure 3a. At low temperatures ($T \leqslant 30$ K), large, nonsaturating MR values are obtained, reaching 1860% at 3 K and 14 T. For $T \geqslant 100$ K the variation of MR with the magnetic field is quite similar to that observed in traditional metal materials. MR decreases to 11% at T = 300 K and B = 14 T. At T = 3 K the MR curve follows a quadratic field-dependent behavior at the low-field region while almost linear at the high-field region. Interestingly, one can find a trace of resistivity oscillations in the low-temperature region, e.g., 3−30 K, which is known as SdH oscillations. To extract the oscillatory component $\Delta\rho$, a smooth background is subtracted from the MR curves. As shown in Figure 3b, the oscillations are still clear at 30 K. One can find that the oscillation patterns which show obviously multifrequency behaviors only varies in amplitude at different temperatures. We employed fast Fourier transform (FFT) to analyze the oscillation frequencies, which

DOI: 10.1021/acsaelm.9b00061
ACS Appl. Electron. Mater. 2019, 1, 869−876

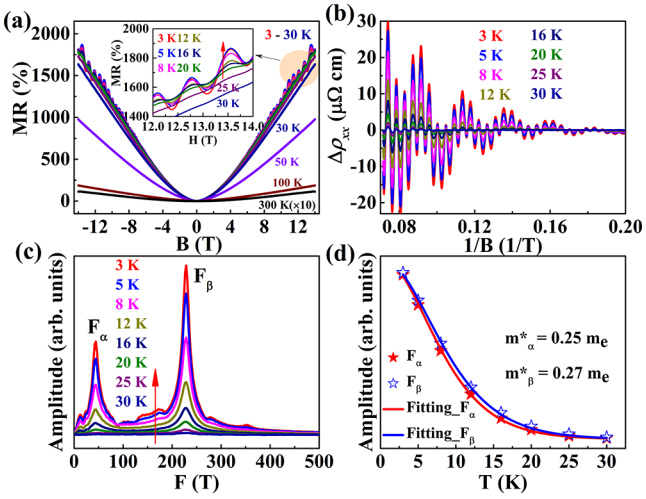

Figure 3. Magnetoresistance and SdH oscillations at different fixed temperatures. (a) Magnetoresistance plotted as a function of magnetic field at different fixed temperatures for the ZrGeSe crystal. Note that the MR curve at 300 K is enlarged by 10 times to present the parabolic behaviors. Insets: zoom-in plot of the oscillation patterns from 3 to 30 K. (b) Oscillation patterns plotted as a function of $1/T$ by extracting from the MR data in (a). (c) FFT spectra with two oscillation frequencies for the SdH oscillations. (d) FFT amplitudes fitting using the L−K formula to obtain the effective mass of the carriers.

are shown in Figure 3c. The SdH oscillations are composed of one lower frequency F_α (= 44.3 T) and a higher frequency F_β (= 228.3 T) for the $\boldsymbol{B}$||c-axis. The coexistence of lower and higher frequencies has also been observed in ZrSiS and HfSiS,[23−27] which suggests that two pockets with obvious different size can be detected from the c-direction in ZrSiS-type nodal-line semimetals. In Hu's work,[31] one more pocket near 400 T also contributes to dHvA oscillations, which is absent in our experiment. The missing pocket in the present SdH oscillations is probably due to the lower (than Hu's work) applied magnetic field, which is a failure to detect the large pocket.

The SdH oscillations for a semimetal can be described by the Lifshitz−Kosevich (L−K) formula,[44] with the Berry phase being taken into account for a topological system:[45]

$$\frac{\Delta\rho}{\rho(0)} = \frac{5}{2}\left(\frac{B}{2F}\right)^{1/2} R_T R_D R_S \cos\left[2\pi\left(\frac{F}{B} + \gamma - \delta\right)\right]$$

where $R_T = \alpha T\mu/B \sinh(\alpha T\mu/B)$, $R_D = \exp(-\alpha T_D\mu/B)$, and $R_S = \cos(\alpha g\mu/2)$. Here, $\mu = m^*/m_0$ is the ratio of effective cyclotron mass m^* to free electron mass m_0, T_D is the Dingle temperature, and $\alpha = (2\pi^2 k_B m_0)/\hbar e$. The oscillations of $\Delta\rho$ is described by the sine term with a phase factor $\gamma - \delta$, in which $\gamma = 1/2 - \Phi_B/2$, and Φ_B is the Berry phase. From the L−K formula, the effective mass of carrier contributing to the SdH effect can be obtained through the fitting of the temperature dependence of oscillation amplitude to the thermal damping factor R_T. In the case of multifrequency oscillations, the oscillation amplitude for each frequency can be represented by the amplitude of the FFT peak. The parameter $1/B$ in R_T should be the average inverse field $1/B$, defined as $1/B = (1/B_{max} + 1/B_{min})/2$. As shown in Figure 3d, for both the low and high frequencies the obtained effective masses are $0.25m_0$ and $0.27m_0$, respectively, which are similar to the results obtained from the dHvA oscillations.[26,31] We also measured the longitude magnetoresistance with the direction of the magnetic field parallel to the current direction. The magnetoresistance is positive and 1 order of magnitude smaller than the transverse one, and it still shows clear signs of Shubnikov−de Haas oscillations at low temperatures (Figure S3).

Because of the multifrequency nature of the oscillations, we fitted the oscillation patterns employing the multifrequency L−K formula (Figure 4a) and obtained the phase shift factor γ −

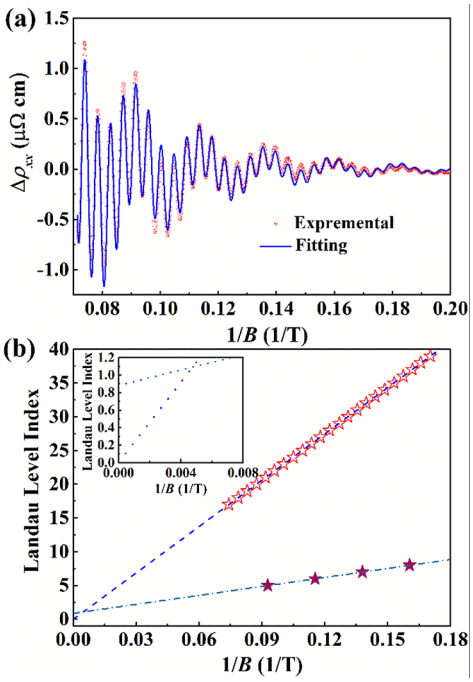

Figure 4. Analyses of the SdH oscillations at 3 K. (a) Fitting of the oscillation patterns at 3 K using the L−K formula. (b) Landau fan diagram of both oscillation patterns. Inset: zoom-in plot of linear fitting lines.

δ related to the two oscillation frequencies 0.93 and 1.08, respectively. Thus, the Berry phase would be $(0.86 \pm 0.25)\pi$ and $(1.14 \pm 0.25)\pi$, respectively. According to the Onsager−Lifshitz equation, $F = (\varphi_0/2\pi^2)A_F$, where A_F is the external area of the cross section of the Fermi surface perpendicular to the magnetic field and φ_0 is the magnetic flux quantum. The cross sections related to the 44.3 and 228.3 T pockets are 4.2×10^{-3} and 21.8×10^{-3} Å^{-2}, respectively. To determine the approximate value of the carrier density for the Fermi pockets, we used its relation with the oscillation frequency, $\Delta\left(\frac{1}{B}\right) = \frac{2e}{\hbar}\left(\frac{g_s g_v}{6\pi^2 n}\right)^{2/3}$, where g_s and g_v are spin and valley degeneracies, respectively. From the magnetic-field-induced damping of oscillation amplitude (Figure 4a), $\Delta\rho \propto \exp\left(-\frac{2\pi^2 k_B m^* T_D}{\hbar e B}\right)$, the Dingle temperature T_D is 3.6 and 7.9 K which are related to the large and small Fermi pockets, respectively. To obtain a quantitative estimate of the carrier mobility, we calculated the quantum mobility, $\mu_q = e/2\pi k_B m^* T_D$. The aforementioned parameters are shown in Table 1.

Another approach to obtain the Berry phase is through the Landau fan diagram, which is shown in Figure 4b. Because $\rho_{xx} > \rho_{xy}$, we assign the maxima of the SdH oscillations as integers (n) at the Landau level to linearly fit the n versus $1/H$ curve.

DOI: 10.1021/acsaelm.9b00061
ACS Appl. Electron. Mater. 2019, 1, 869−876

Table 1. Parameters Extracted from SdH Oscillations for Two Fermi Pockets[a]

F (T)	A_F (10^{-3} Å^{-2})	m^* (m_0)	n_q (10^{18} cm^3)	μ_q (10^3 cm^2/(V s))	Φ (π)
44.3	4.2	0.25	1.6	2.3	0.86 ± 0.25
228.3	21.3	0.27	19	1.1	1.14 ± 0.25

[a] A_F and Φ are the cross section area of the Fermi surface and the Berry phase of the Fermi pockets, respectively.

As one can see in the inset of Figure 4b, the y-axis-intercept values of 0.85 and 0.03 are obtained for the 44.3 and 228.3 T pockets, respectively, illustrating the nontrivial Berry phase in the transport behaviors.

Angle-Dependent SdH Oscillations. To further understand the geometry of Fermi surface, we performed angle-resolved SdH oscillations measurements. The MR versus B curves, as measured at different orientations of magnetic fields, are shown in Figure 5a, where the magnetic field is always

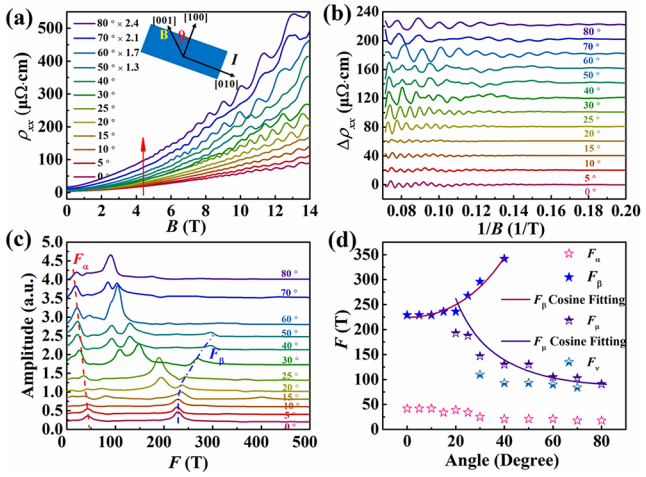

Figure 5. Angle-dependent SdH oscillations. (a) Resistivity plotted as a function of the magnetic field for various angles at T = 3 K. To present all of the oscillation patterns without overlap, we multiply the 50°−80° data with different constants. (b) Oscillation patterns at different angles plotted with $1/T$ by subtracting the smooth background of MR curves in (a). (c) FFT patterns of the oscillation parts extracted from the MR curves. (d) Oscillation frequencies evolve with the rotation angle.

perpendicular to the current or the b-axis of the crystal to ignore the influences of the angle between the magnetic field and the current (see the schematic diagram shown in the inset of Figure 5a). The rotation parameter θ is the angle between the c-axis and the direction of the magnetic field. Namely, the rotation of the direction of magnetic field is always within the ac-plane. As the direction of the magnetic field rotates toward the ab-plane, MR increases gradually before 45° and then decreases with further increase in θ. In fact, the MR values at certain magnetic field (e.g., 14 T) forms a "butterfly" shape (Figure S4). The 4-fold-like symmetry of the angle-dependent MR curve at a fixed magnetic field implies that the Fermi surface of the ZrGeSe crystal is three-dimensional.[46] To clearly demonstrate the oscillations in the angle-dependent MR curves, we multiply the higher than 50° data with different constants to demonstrate the increasing tendency. It can be seen that the oscillation patterns change near 45°. By subtracting the smooth background, we extract the oscillation patterns for all the rotation angles (Figure 5b), which implies that the Fermi surface of ZrGeSe is formed by several components from different directions. The FFT spectra related to the oscillations are shown in Figure 5c. The F_α frequency slightly changes with the rotating angle, from 44.3 T at 0° to 21 T at 80°, while the F_β frequency shows a 2-D-like behavior, which increases roughly in the $1/\cos\theta$ form and vanishes at about 60°, as shown by the fitting line in Figure 5d. New frequencies (F_μ and F_ν) can be found during the rotating process, which are slightly angle dependent. We roughly fit F_μ with cosine relationship in the 30°−80° region. Although the two frequencies F_μ and F_ν seem like Zeeman splitting peaks, which was previously found in ZrSiS[39] under low magnetic fields, e.g., 5 T, we should be more careful in the absence of Zeeman splitting in dHvA results.[31] Therefore, we employ first-principles calculations to theoretically analyze the Fermi surface of ZrGeSe.

DFT Calculation. To further understand the electronic properties of the ZrGeSe crystal, first-principles calculations are performed based on the density functional theory (DFT). The optimized lattice constants from the DFT calculations are $a = b$ = 3.6891 Å and c = 8.264 Å. These values are quite close to the experimental ones ($a = b$ = 3.69 Å, c = 8.24 Å at 300 K). According to the density of states (DOS), the bands near the Fermi level are contributed by highly hybridized Zr 4d orbitals, Ge 4p orbitals, and Se 4p orbitals, as shown in Figure 6a. The

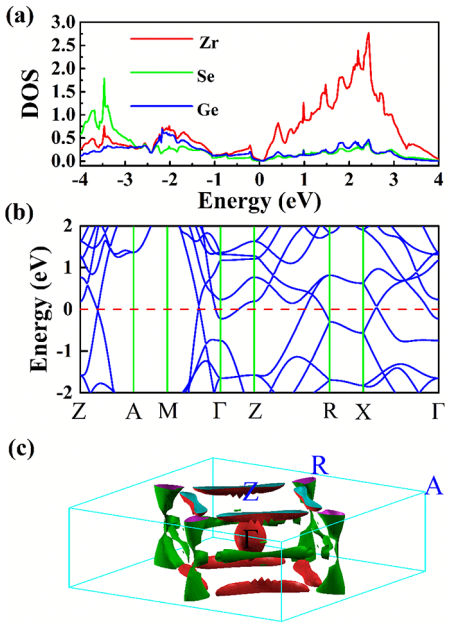

Figure 6. Calculated band structure and Fermi surface of ZrGeSe. (a) Density of states. (b) Band structure. (c) 3D Fermi surfaces of ZrGeSe in the reciprocal space.

band structure displayed in Figure 6b confirms the Dirac-like feature at the Fermi level. We also plot the calculated 3D Fermi surface in Figure 6c, which shows similar morphology with other ZrSiS-type topological nodal-line semimetals. However, an obvious difference between ZrGeSe and ZrSiS is the electron pocket at the center of the Brillouin zone Γ, which is formed by normal bands rather than Dirac bands. Upon application of magnetic fields along the c-axis only two oscillations can be detected, which correspond to the two Dirac bands at $Z-A$ and $Z-R$ directions. The large pocket at

DOI: 10.1021/acsaelm.9b00061
ACS Appl. Electron. Mater. 2019, 1, 869−876

Γ, which is however not even traceable, might due to the low carrier's mobility and its higher quantized field. The pocket at Γ brings more electron carriers in ZrGeSe, resulting in ZrGeSe's electron dominant Hall behaviors shown in Figure S5 (ZrSiS is hole dominant[39]). The obtained carriers' mobility is about 1000 $cm^2\ V^{-1}\ s^{-1}$ at low temperature from Hall measurements, which is of the same magnitude as, however slightly smaller than, the quantum mobility. It is reliable that the carrier's mobility of normal band around Γ point would be significantly smaller than those of Dirac bands. Namely, the Dirac bands still dominant magnetotransport behaviors, resulting in the large unsaturated MR effect as well as SdH oscillations in both MR and Hall effect measurements.

In Figure 6c, the famous nodal ring of ZrSiS-type nodal-line semimetal can be found in the ZrGeSe near the $Z-A-R$ plane, which is more or less 2D-like, and contributes to the quasi-2D-like behavior in angle-dependent SdH analyses. Moreover, one can find another nodal ring at the middle plane of the Brillouin zone, which is slightly different in size. This nodal ring may contribute to the multifrequency oscillation patterns in the angle-dependent experiments.

4. CONCLUSIONS

In summary, high quality ZrGeSe single crystals were synthesized via the chemical vapor transport. Electronic transport measurements show that the ZrGeSe single crystal exhibits metallic conductivity down to 3 K and resistivity plateaus below T = 10 K for $B \geqslant 3$ T, whose magnitude is strongly enhanced by the application of magnetic fields with its direction perpendicular to the electric current direction. Upon sweeping the magnetic field at T = 3 K, the ZrGeSe crystals show large positive magnetoresistance (1.86×10^3%) with quantum oscillations in the high-field region. The analyses of SdH quantum oscillations data reveal properties consistent with the theoretically predicted topological semimetal state. Combining angle-dependent SdH oscillations and DFT calculations, we deduce that the Fermi surface of the ZrGeSe is constructed by normal bands and Dirac bands. The latter plays the dominant role in determining the magnetotransport behaviors. All these findings demonstrate that ZrGeSe is one of good nodal-line semimetals for further theoretical and experimental investigations.

■ ASSOCIATED CONTENT

Supporting Information

The Supporting Information is available free of charge on the ACS Publications website at DOI: 10.1021/acsaelm.9b00061.

X-ray energy dispersive spectroscopy (EDS) elemental mapping of Zr, Ge, and Se, temperature dependence of the resistivity in zero magnetic field together with the fitting of the resistivity using equation $\rho(T) = \rho_0 + AT^n$, longitudinal magnetoresistance as a function of the magnetic field at different fixed temperatures, polar plots of angle-dependent normalized resistivity at T = 3 K and in magnetic fields of B = 4, 9, and 14 T, and the Hall resistance as a function of the magnetic field at different fixed temperatures for the ZrGeSe single crystal; Kohler's plot of magnetoresistance at different temperatures (PDF)

■ AUTHOR INFORMATION

Corresponding Authors

*E-mail: zrk@ustc.edu (R.K.Z.).
*E-mail: sdong@seu.edu.cn (S.D.).
*E-mail: wz929@uowmail.edu.au (W.Z.).

ORCID

Xiao-Guang Li: 0000-0003-4016-4483
Shuai Dong: 0000-0002-6910-6319
Ren-Kui Zheng: 0000-0002-8897-703X

Author Contributions

L.G. and T.-W.C. contributed equally to this work.

Notes

The authors declare no competing financial interest.

■ ACKNOWLEDGMENTS

This work was supported by the National Natural Science Foundation of China (Grants 51572278, 51790491, 51872278, and 11674055) and the National Key Research and Development Plan (Grants 2016YFA0300103 and 2015CB921201). Support from Jiangxi Key Laboratory for Two-Dimensional Materials is also acknowledged. W.Z. and L.C. acknowledge the scholarship supporting from UOW.

■ REFERENCES

(1) Hasan, M. Z.; Kane, C. L. Colloquium: topological insulators. *Rev. Mod. Phys.* **2010**, *82*, 3045.
(2) Qi, X. L.; Zhang, S. C. Topological insulators and superconductors. *Rev. Mod. Phys.* **2011**, *83*, 1057.
(3) Wang, Z. J.; Sun, Y.; Chen, X. Q.; Franchini, C.; Xu, G.; Weng, H. M.; Dai, X.; Fang, Z. Dirac semimetal and topological phase transitions in A_3Bi (A = Na, K, Rb). *Phys. Rev. B: Condens. Matter Mater. Phys.* **2012**, *85*, 195320.
(4) Wang, Z.; Weng, H.; Wu, Q.; Dai, Xi.; Fang, Z. Three dimensional Dirac semimetal and quantum transport in Cd_3As_2. *Phys. Rev. B: Condens. Matter Mater. Phys.* **2013**, *88*, 125427.
(5) Wolf, S. A.; Awschalom, D. D.; Buhrman, R. A.; Daughton, J. M.; von Molnár, S.; Roukes, M. L.; Chtchelkanova, A. Y.; Treger, D. M. Spintronics: A Spin-Based Electronics Vision for the Future. *Science* **2001**, *294*, 1488.
(6) Shekhar, C.; Nayak, A. K.; Sun, Y.; Schmidt, M.; Nicklas, M.; Leermakers, I.; Zeitler, U.; Skourski, Y.; Wosnitza, J.; Liu, Z.; Chen, Y.; Schnelle, W.; Borrmann, H.; Grin, Y.; Felser, C.; Yan, B. Extremely large magnetoresistance and ultrahigh mobility in the topological Weyl semimetal candidate NbP. *Nat. Phys.* **2015**, *11*, 645.
(7) Liu, Z. K.; Jiang, J.; Zhou, B.; Wang, Z. J.; Zhang, Y.; Weng, H. M.; Prabhakaran, D.; Mo, S. K.; Peng, H.; Dudin, P.; Kim, T.; Hoesch, M.; Fang, Z.; Dai, X.; Shen, Z. X.; Feng, D. L.; Hussain, Z.; Chen, Y. L. A stable three-dimensional topological Dirac semimetal Cd_3As_2. *Nat. Mater.* **2014**, *13*, 677.
(8) Xia, Y.; Qian, D.; Hsieh, D.; Wray, L.; Pal, A.; Lin, H.; Bansil, A.; Grauer, D.; Hor, Y. S.; Cava, R. J.; Hasan, M. Z. Observation of a large-gap topological-insulator class with a single Dirac cone on the surface. *Nat. Phys.* **2009**, *5*, 398−402.
(9) Xu, S. Y.; Belopolski, I.; Alidoust, N.; Neupane, M.; Bian, G.; Zhang, C. L.; Sankar, R.; Chang, G. Q.; Yuan, Z. J.; Lee, C. C.; Huang, S. M.; Zheng, H.; Ma, J.; Sanchez, D. S.; Wang, B. K.; Bansil, A.; Chou, F. C.; Shibayev, P. P.; Lin, H.; Jia, S.; Hasan, M. Z. Discovery of a Weyl fermion semimetal and topological Fermi arcs. *Science* **2015**, *349*, 613.
(10) Kim, Y.; Wieder, B. J.; Kane, C. L.; Rappe, A. M. Dirac Line Nodes in Inversion-Symmetric Crystals. *Phys. Rev. Lett.* **2015**, *115*, No. 036806.
(11) Weng, H.; Liang, Y.; Xu, Q.; Yu, R.; Fang, Z.; Dai, X.; Kawazoe, Y. Topological node-line semimetal in three-dimensional graphene

DOI: 10.1021/acsaelm.9b00061
ACS Appl. Electron. Mater. 2019, 1, 869−876

networks. *Phys. Rev. B: Condens. Matter Mater. Phys.* **2015**, *92*, No. 045108.
(12) Fang, C.; Weng, H. M.; Dai, X.; Fang, Z. Topological nodal line semimetals. *Chin. Phys. B* **2016**, *25*, 117106.
(13) Fang, C.; Chen, Y.; Kee, H. Y.; Fu, L. Topological nodal line semimetals with and without spin-orbital coupling. *Phys. Rev. B: Condens. Matter Mater. Phys.* **2015**, *92*, No. 081201.
(14) Xu, Q. N.; Yu, R.; Fang, Z.; Dai, X.; Weng, H. M. Topological nodal line semimetals in the CaP_3 family of materials. *Phys. Rev. B: Condens. Matter Mater. Phys.* **2017**, *95*, No. 045136.
(15) Chan, Y. H.; Chiu, C. K.; Chou, M. Y.; Schnyder, A. P. Ca_3P_2 and other topological semimetals with line nodes and drumhead surface states. *Phys. Rev. B: Condens. Matter Mater. Phys.* **2016**, *93*, 205132.
(16) Niu, C. W.; Buhl, P. M.; Bihlmayer, G.; Wortmann, D.; Dai, Y.; Blügel, S.; Mokrousov, Y. Two-dimensional topological nodal line semimetal in layered X_2Y (X = Ca, Sr, and Ba; Y = As, Sb, and Bi). *Phys. Rev. B: Condens. Matter Mater. Phys.* **2017**, *95*, 235138.
(17) Zhang, X. M.; Jin, L.; Dai, X. F.; Liu, G. D. Topological Type-II Nodal Line Semimetal and Dirac Semimetal State in Stable Kagome Compound Mg_3Bi_2. *J. Phys. Chem. Lett.* **2017**, *8*, 4814−4819.
(18) Zeng, M. G.; Fang, C.; Chang, G. Q.; Chen, Y. A., Hsieh, T.; Bansil, A.; Lin, H.; Fu, L. Topological semimetals and topological insulators in rare earth monopnictides. arXiv:1504.03492.
(19) Kim, Y. K.; Wieder, B. J.; Kane, C. L.; Rappe, A. M. Dirac line nodes in inversion-symmetric crystals. *Phys. Rev. Lett.* **2015**, *115*, No. 036806.
(20) Yu, R.; Weng, H. M.; Fang, Z.; Dai, X.; Hu, X. Topological node-line semimetal and Dirac semimetal state in antiperovskite Cu_3PdN. *Phys. Rev. Lett.* **2015**, *115*, No. 036807.
(21) Bian, G.; Chang, T. R.; Zheng, H.; Velury, S.; Xu, S. Y.; Neupert, T.; Chiu, C. K.; Huang, S. M.; Sanchez, D. S.; Belopolski, I.; Alidoust, N.; Chen, P. J.; Chang, G. Q.; Bansil, A.; Jeng, H. T.; Lin, H.; Hasan, M. Z. Drumhead surface states and topological nodal-line fermions in $TlTaSe_2$. *Phys. Rev. B: Condens. Matter Mater. Phys.* **2016**, *93*, 121113.
(22) Bian, G.; Chang, T. R.; Sankar, R.; Xu, S. Y.; Zheng, H.; Neupert, T.; Chiu, C. K.; Huang, S. M.; Chang, G. Q.; Belopolski, I.; Sanchez, D. S.; Neupane, M.; Alidoust, N.; Liu, C.; Wang, B. K.; Lee, C. C.; Jeng, H. T.; Yuan, Z. J.; Jia, S.; Bansil, A.; Chou, F. C.; Lin, H.; Hasan, M. Z. Topological nodal-line fermions in spin-orbit metal $PbTaSe_2$. *Nat. Commun.* **2016**, *7*, 10556.
(23) Neupane, M.; Belopolski, I.; Hosen, M. M.; Sanchez, D. S.; Sankar, R.; Szlawska, M.; Xu, S. Y.; Dimitri, K.; Dhakal, N.; Maldonado, P.; Oppeneer, P. M.; Kaczorowski, D.; Chou, F. C.; Hasan, M. Z.; Durakiewicz, T. Observation of topological nodal fermion semimetal phase in ZrSiS. *Phys. Rev. B: Condens. Matter Mater. Phys.* **2016**, *93*, 201104.
(24) Chen, C.; Xu, X.; Jiang, J.; Wu, S. C.; Qi, Y. P.; Yang, L. X.; Wang, M. X.; Sun, Y. N.; Schroter, B. M.; Yang, H. F.; Schoop, L. M.; Lv, Y. Y.; Zhou, J.; Chen, Y. B.; Yao, S. H.; Lu, M. H.; Chen, Y. F.; Felser, C.; Yan, B. H.; Liu, Z. K.; Chen, Y. L. Dirac line nodes and effect of spin-orbit coupling in the nonsymmorphic critical semimetals MSiS (M = Hf, Zr). *Phys. Rev. B: Condens. Matter Mater. Phys.* **2017**, *95*, 125126.
(25) Hosen, M.; Dimitri, K.; Belopolski, I.; Maldonado, P.; Sankar, R.; Dhakal, N.; Dhakal, G.; Cole, T.; Oppeneer, P. M.; Kaczorowski, D.; Chou, F. C.; Hasan, M. Z.; Durakiewicz, T.; Neupane, M. Tunability of the topological nodal-line semimetal phase in ZrSiX-type materials (X= S, Se, Te). *Phys. Rev. B: Condens. Matter Mater. Phys.* **2017**, *95*, 161101.
(26) Hu, J.; Tang, Z. J.; Liu, J. Y.; Zhu, Y. L.; Wei, J.; Mao, Z. Q. Nearly massless Dirac fermions and strong Zeeman splitting in the nodal-line semimetal ZrSiS probed by de Haas−van Alphen quantum oscillations. *Phys. Rev. B: Condens. Matter Mater. Phys.* **2017**, *96*, No. 045127.
(27) Schoop, L. M.; Ali, M. N.; Straßer, C.; Topp, A.; Varykhalov, A.; Marchenko, D.; Duppel, V.; Parkin, S. S. P.; Lotsch, B. V.; Ast, C. R. Dirac cone protected by non-symmorphic symmetry and three-dimensional Dirac line node in ZrSiS. *Nat. Commun.* **2016**, *7*, 11696.
(28) Emmanouilidou, E. E.; Shen, B.; Deng, X. Y.; Chang, T. R.; Shi, A. S.; Kotliar, G.; Xu, S. Y.; Ni, N. Magnetotransport properties of the single-crystalline nodal-line semimetal candidates CaTX (T= Ag, Cd; X= As, Ge). *Phys. Rev. B: Condens. Matter Mater. Phys.* **2017**, *95*, 245113.
(29) Liang, Q. F.; Zhou, J.; Yu, R.; Wang, Z.; Weng, H. M. Node-surface and node-line fermions from nonsymmorphic lattice symmetries. *Phys. Rev. B: Condens. Matter Mater. Phys.* **2016**, *93*, No. 085427.
(30) Hu, J.; Tang, Z. J.; Liu, J. Y.; Liu, X.; Zhu, Y. L.; Graf, D.; Myhro, K.; Tran, S.; Lau, C. N.; Wei, J.; Mao, Z. Q. Evidence of topological nodal-line fermions in ZrSiSe and ZrSiTe. *Phys. Rev. Lett.* **2016**, *117*, No. 016602.
(31) Hu, J.; Zhu, Y. L.; Graf, D.; Tang, Z. J.; Liu, J. Y.; Mao, Z. Q. Quantum oscillation studies of the topological semimetal candidate ZrGeM (M= S, Se, Te). *Phys. Rev. B: Condens. Matter Mater. Phys.* **2017**, *95*, 205134.
(32) Hu, J.; Zhu, Y. L.; Gui, X.; Graf, D.; Tang, Z. J.; Xie, W. W.; Mao, Z. Q. Quantum oscillation evidence for a topological semimetal phase in ZrSnTe. *Phys. Rev. B: Condens. Matter Mater. Phys.* **2018**, *97*, 155101.
(33) Kresse, G.; Joubert, D. From ultrasoft pseudopotentials to the projector augmented-wave method. *Phys. Rev. B: Condens. Matter Mater. Phys.* **1999**, *59*, 1758.
(34) Blöchl, P. E. Projector augmented-wave method. *Phys. Rev. B: Condens. Matter Mater. Phys.* **1994**, *50*, 17953.
(35) Perdew, J. P.; Ruzsinszky, A.; Csonka, G. I.; Vydrov, O. A.; Scuseria, G. E.; Constantin, L. A.; Zhou, X. L.; Burke, K. Restoring the density-gradient expansion for exchange in solids and surfaces. *Phys. Rev. Lett.* **2008**, *100*, 136406.
(36) Wang, V.; Liu, Y. C.; Kawazoe, Y.; Geng, W. T. Role of interlayer coupling on the evolution of band edges in few-layer phosphorene. *J. Phys. Chem. Lett.* **2015**, *6*, 4876−4883.
(37) Xu, Q.; Song, Z.; Nie, S.; Weng, H.; Fang, Z.; Dai, X. Two-dimensional oxide topological insulator with iron-pnictide superconductor LiFeAs structure. *Phys. Rev. B: Condens. Matter Mater. Phys.* **2015**, *92*, 205310.
(38) Liang, T.; Gibson, Q.; Ali, M. N.; Liu, M. H.; Cava, R. J.; Ong, N. P. Ultrahigh mobility and giant magnetoresistance in the Dirac semimetal Cd_3As_2. *Nat. Mater.* **2015**, *14*, 280−284.
(39) Singha, R.; Pariari, A. K.; Satpati, B.; Mandal, P. Large nonsaturating magnetoresistance and signature of nondegenerate Dirac nodes in ZrSiS. *Proc. Natl. Acad. Sci. U. S. A.* **2017**, *114*, 2468−2473.
(40) Ziman, J. M. *Electrons and Phonons: The Theory of Transport Phenomena in Solids*; Oxford University Press: 1960.
(41) Guo, L.; Liu, Y.-K.; Gao, G.-Y.; Huang, Y.-Y.; Gao, H.; Chen, L.; Zhao, W.; Ren, W.; Li, S.-Y.; Li, X.-G.; Dong, S.; Zheng, R.-K. Extreme magnetoresistance and SdH oscillation in compensated semimetals of $NbSb_2$ single crystals. *J. Appl. Phys.* **2018**, *123*, 155103.
(42) Wang, Y. L.; Thoutam, L. R.; Xiao, Z. L.; Hu, J.; Das, S.; Mao, Z. Q.; Wei, L.; Divan, R.; Luican-Mayer, A.; Crabtree, G. W.; Kwok, W. K. Origin of the turn-on temperature behavior in WTe_2. *Phys. Rev. B: Condens. Matter Mater. Phys.* **2015**, *92*, 180402.
(43) Jo, N. H.; Wu, Y.; Wang, L.-L.; Orth, P. P.; Downing, S. S.; Manni, S.; Mou, D.; Johnson, D. D.; Kaminski, A.; Bud'ko, S. L.; Canfield, P. C. Extremely large magnetoresistance and Kohler's rule in PdSn4: a complete study of thermodynamic, transport, and band-structure properties. *Phys. Rev. B: Condens. Matter Mater. Phys.* **2017**, *96*, 165145.
(44) Lifshitz, I. M.; Kosevich, A. M. Theory of magnetic susceptibility in metals at low temperatures. *Sov. Phys. JETP* **1956**, *2*, 636−645.
(45) Mikitik, G. P.; Sharlai, Y. V. Manifestation of Berry's phase in metal physics. *Phys. Rev. Lett.* **1999**, *82*, 2147.

DOI: 10.1021/acsaelm.9b00061
ACS Appl. Electron. Mater. 2019, 1, 869−876

(46) Topp, A.; Lippmann, J. M.; Varykhalov, A.; Duppel, V.; Lotsch, B. V.; Ast, C. R.; Schoop, L. M. Non-symmorphic band degeneracy at the Fermi level in ZrSiTe. *New J. Phys.* **2016**, *18*, 125014.

DOI: 10.1021/acsaelm.9b00061
ACS Appl. Electron. Mater. 2019, 1, 869−876